TU Delft

Delft University of Technology

Document Version
Final published version

Licence
Dutch Copyright Act (Article 25fa)

Citation (APA)
Shinde, S., Rituraj, G., Mouli, G. R. C., Iyer, V. M., & Bauer, P. (2026). Integrated Magnetic Structure to Improve High Power Region Efficiency for Dual Active Bridge Converter. *IEEE Journal of Emerging and Selected Topics in Industrial Electronics*, *7*(2), 498-510. https://doi.org/10.1109/JESTIE.2025.3648204

Important note
To cite this publication, please use the final published version (if applicable).
Please check the document version above.

Copyright
In case the licence states “Dutch Copyright Act (Article 25fa)”, this publication was made available Green Open Access via the TU Delft Institutional Repository pursuant to Dutch Copyright Act (Article 25fa, the Taverne amendment). This provision does not affect copyright ownership.
Unless copyright is transferred by contract or statute, it remains with the copyright holder.

Sharing and reuse
Other than for strictly personal use, it is not permitted to download, forward or distribute the text or part of it, without the consent of the author(s) and/or copyright holder(s), unless the work is under an open content license such as Creative Commons.

Takedown policy
Please contact us and provide details if you believe this document breaches copyrights.
We will remove access to the work immediately and investigate your claim.

This work is downloaded from Delft University of Technology.

Integrated Magnetic Structure to Improve High Power Region Efficiency for Dual Active Bridge Converter

Siddhesh Shinde, *Graduate Student Member, IEEE*, Gautam Rituraj, *Member, IEEE*, Gautham Ram Chandra Mouli, *Senior Member, IEEE*, Vishnu Mahadeva Iyer, *Senior Member, IEEE*, and Pavol Bauer, *Senior Member, IEEE*

***Abstract*—In dual active bridge (DAB) converters, series inductor and transformer functionalities are integrated into a single magnetic core structure to improve efficiency or power density. Allowing independent tuning of this integrated series inductance and magnetizing inductance gives higher design flexibility. However, the existing integrated magnetic methods often lower magnetizing inductance, compromise the transformer winding coupling, require complex custom core designs, or cannot effectively decouple transformer and inductor fluxes in the case of separate transformer and inductor windings. To overcome these problems, this article proposes a unified core structure that allows independent tuning of series inductance without the above-mentioned limitations. To demonstrate the performance of the proposed integrated structure, a DAB converter for a dc–dc electric vehicle charging application is built, and the proposed integrated structure is compared with discrete transformer and inductor structures under identical core volume and thermal steady-state conditions. It is experimentally validated that for the proposed structure at a high output voltage and high load conditions of 450 V and 9 kW, the magnetic power loss reduction is 8.8%, whereas, at a low output voltage and high load conditions of 250 V and 7 kW, the magnetic power loss reduction is 13.0%. Furthermore, this article presents an iterative design methodology based on the derived reluctance and analytical models to systematize the design process.**

***Index Terms*—Dual active bridge (DAB), ferrite, integrated inductor transformer (ILX), integrated magnetics, reluctance modeling.**

I. Introduction

THE widespread adoption of electric vehicles (EVs) is projected to significantly reduce CO_2 emissions. This has led to a significant increase in research and development toward building efficient, low-cost, and compact power electronics for EV charging. The mainstream use of wide band gap devices, which leads to compact and efficient designs of power electronics, has necessitated advancements in magnetic design, such as integrated magnetic structures that combine multiple magnetic components.

A DAB converter is one of the topologies used in the dc–dc stage of EV chargers. The design of the series inductor and transformer components is critical in this topology. Higher magnetizing inductance can reduce the magnetizing current component, reducing the core losses and the current stress on the switches. Consequently, high coupling between the transformer windings reduces the leakage field and, therefore, the loss in these windings. Meanwhile, the value of the series inductance influences the power flow characteristics of DAB. Therefore, in integrated magnetics, the ability to tune the series inductance without reducing the magnetizing inductance or reducing the coupling of transformer windings provides higher design flexibility.

Several methods can be found in the literature to effectively integrate series inductor and transformer functionality in a single-core structure to reduce the volume of the magnetic component or reduce the loss dissipation. These methods can be generally classified into three different categories; method-1: Utilizing the leakage inductance by spacing windings [1], [2], [3], [4], [5], method-2: Mimicking leakage inductance by providing a controlled leakage flux path within the magnetic core structure [4], [6], [7], [8], [9], [10], [11], and method-3: Separate inductor and transformer winding wound on the same core structure with decoupled fluxes [12], [13], [14], [15], [16].

In the first method [1], [2], [3], [4], the leakage inductance is created by spacing primary and secondary windings; the value of leakage inductance is limited to interwinding spacing constraints. If the primary and secondary windings are placed far apart, this method results in poor coupling and reduction of magnetizing inductance. In [5], the transformer's primary and secondary windings are put in sections where a leakage inductance is controlled by spacing between the primary and secondary windings by properly breaking the interleaving. In this sectional winding method, it is demonstrated that the winding losses scale up with a higher leakage inductance value.

In the second type of magnetic integration method, Pavlovsky et al. [6] showed how to utilize the leakage layer made up of high-permeability material to contain the leakage fluxes. Even though this method leads to reasonable control of the leakage inductance, it increases core manufacturing complexity and the

Received 9 May 2025; revised 24 September 2025 and 25 November 2025; accepted 18 December 2025. Date of publication 24 December 2025; date of current version 26 March 2026. The work was supported by Top Sector Energy subsidy from the Ministry of Economic Affairs and Climate, carried out by the Netherlands Enterprise Agency (RVO), through the specific subsidy for this project concerns the MOOI subsidy round 2020. *(Corresponding author: Siddhesh Shinde.)*

Siddhesh Shinde, Gautam Rituraj, Gautham Ram Chandra Mouli, and Pavol Bauer are with the Department of Electrical Sustainable Energy, Delft University of Technology, Delft 2628 CD, The Netherlands (e-mail: s.s.shinde-1@tudelft.nl; g.rituraj@tudelft.nl; g.r.chandramouli@tudelft.nl; p.bauer@tudelft.nl).

Vishnu Mahadeva Iyer is with the Department of Electrical Engineering, Indian Institute of Science, Bengaluru, Karnataka 560012, India (e-mail: vishnumi@iisc.ac.in).

Digital Object Identifier 10.1109/JESTIE.2025.3648204

2687-9743 © 2025 IEEE. All rights reserved, including rights for text and data mining, and training of artificial intelligence and similar technologies. Personal use is permitted, but republication/redistribution requires IEEE permission. See https://www.ieee.org/publications/rights/index.html for more information.

Authorized licensed use limited to: TU Delft Library. Downloaded on April 14,2026 at 08:54:41 UTC from IEEE Xplore. Restrictions apply.

TABLE I
COMPARISON OF ILX STRUCTURE AGAINST OTHER STATE-OF-THE-ART

Literature	Transformer coupling	Reduction in L_m	L_e control method	Flux coupling ϕ_{ind} and ϕ_{tx}	Core design	Compared to discrete
Ortiz et al. [1]	Depends on L_e	Yes	Winding space	NA	Standard	NA
Pavlovsky et al. [6]	Depends on L_e	Yes	Leakage layer	NA	Custom	NA
Zhang et al. [7]	Depends on L_e	Yes	Shunt tuning	NA	Standard	NA
Biela et al. [8]	Depends on L_e	Yes	Airgap	NA	Standard	NA
Li et al. [10]	High	No	Middle limb airgap	NA	Standard	8% higher losses
D'Antonio et al. [11]	High	No	Horizontal airgap	NA	Custom	3.45% higher losses
Kim et al. [12]	High	No	Outer turns	Partially	Standard	NA
Ahmed et al. [14]	High	No	Turns and airgap	Weakly	Custom	0.6% higher efficiency
Cao et al. [16]	High	No	I-core airgaps	Conditional	Standard	12.1% reduction in volume
This work	**High**	**No**	**Turns and airgap**	**Weakly**	**Standard**	8.8% to 13% reduction **in losses**

Note: The designs compared in Table I are intended for different applications, each with distinct voltage and power (kVA) specifications.

risk of winding insulation failure. Similarly, in [7], a magnetic shunt is used between primary and secondary windings with an airgap. The shunt provides the path for leakage flux. Alternatively, in [4], [8], and [9], the primary and secondary windings are wound on the outer limbs of the transformer core, and the middle limb with the airgap acts like a controlled leakage path. In the above-mentioned controlled-leakage path methods, when a higher leakage inductance is desired, the coupling is reduced, and the magnetizing inductance is compromised. In addition, the gap causes higher fringing fields and losses in the windings. To overcome the coupling problem, Li et al. [10] proposed a solution where asymmetric primary and secondary windings are wound on each outer leg. This winding arrangement ensures tight coupling and creates leakage flux that flows through the center limb. Airgaps are placed on the central leg to adjust leakage inductance and on the outer legs to adjust magnetizing inductance independently. However, the losses are increased compared to the discrete structure of similar volume due to the increase in winding ac resistance. D'Antonio et al. [11] applied a customized horizontal airgap between the middle and outer right side limb to control leakage inductance. The primary and secondary windings are asymmetrically wound on the outer left and middle limbs. This winding method ensures higher magnetizing inductance. However, placing the horizontal airgap reduces the core utilization.

The third type of magnetic integration method has separate windings for the inductor and transformer functionalities. In [12], the primary winding is split between the middle and outer limbs, whereas the secondary winding is placed only in the middle limb. The inductance is controlled by changing the number of outer primary turns. This method provides higher magnetizing inductance but showcases coupling between the inductor flux and the transformer flux. In addition, the absence of an airgap increases the chances of core saturation. Work by authors of [13] and [14] showed the integration of a resonant inductor with a matrix transformer. Inductor and transformer functionalities are achieved by separate windings, and their fluxes are decoupled. The reduction in core loss is shown due to the flux cancellation effect. Nonetheless, the core structure used in this application is custommade, and both methods rely on the precise layout of the PCB winding to avoid current crowding or current imbalance. Stegen and Lu [15] presented a vertical structure with different inductors and transformer windings. However, due to the coupling of their individual fluxes, a major reduction of efficiency is reported at high power. Cao et al. [16] showed the integrated structure with UU-core forming a transformer connected with two spliced I-cores for the inductor. This structure allows the decoupling of transformer and inductor flux under certain conditions and requires precise alignment of the two I-cores. Furthermore, it is constructed using two different core materials, which have different flux density saturation limits and thermal properties, leading to a more complicated design.

Table I shows the comparison of the proposed integrated magnetic structure against the state-of-the-art integrated magnetics. It is observed that achieving independent control over the series inductor L_e without compromising magnetizing inductance L_m comes with other caveats. These reported methods in the literature either suffer due to coupling between the inductor flux ϕ_{ind} and transformer flux ϕ_{tx} [12], [16], a customized core structure [11], [13], [14], poor core utilization [11], or higher losses [10], [11]. In this context, this work proposes an integrated inductor transformer (ILX) structure for the DAB converter that has the following key contributions.

1) ILX is constructed using off-the-shelf standard cores, that allows independent tuning of L_e without compromising L_m. The design guarantees weak coupling between ϕ_{ind} and ϕ_{tx} and ensures high coupling between transformer windings (see Sections II, V-A, and VI).
2) The iterative design methodology for ILX is proposed to integrate the series inductance and transformer functionality into a single core structure, based on derived reluctance and analytical models (see Sections III and IV).
3) An experimental comparison between the discrete inductor–transformer design and the ILX structure is presented, under identical core volume and steady-state thermal conditions with the focus on verifying predicted core loss reduction (see Sections V-B and VI-C).

The rest of this article is organized as follows. Section II introduces the ILX structure for the DAB converter and discusses the superposition of the fluxes. Section III shows how to construct a

Authorized licensed use limited to: TU Delft Library. Downloaded on April 14,2026 at 08:54:41 UTC from IEEE Xplore. Restrictions apply.

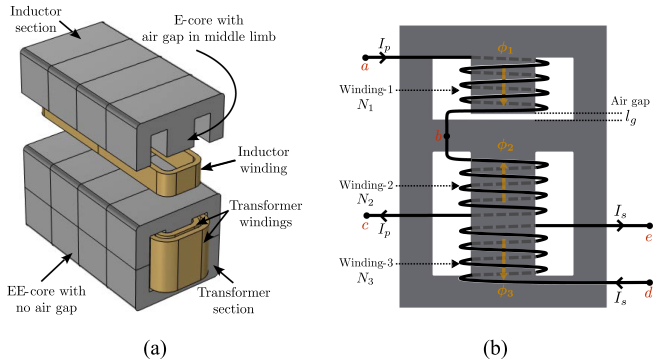

Fig. 1. (a) ILX structure. (b) ILX sense of winding and flux orientation.

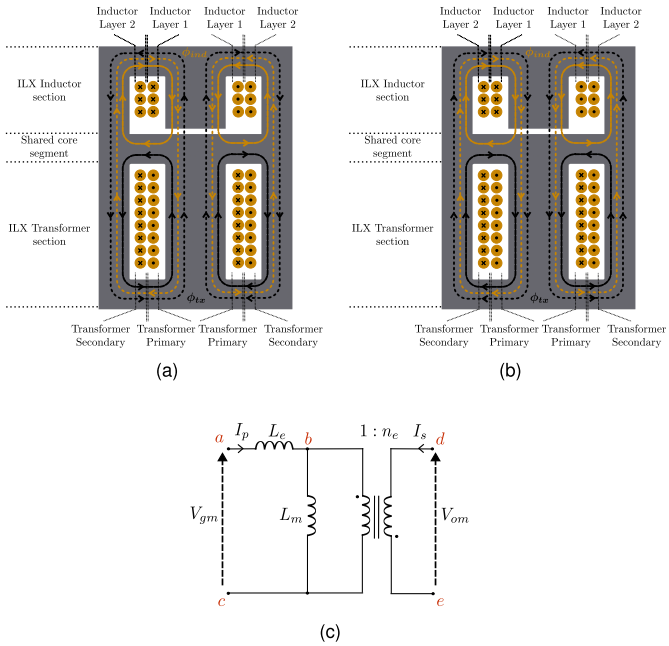

Fig. 2. (a) Scenario-1: magnitude of ϕ_2 greater than the magnitude of ϕ_3. (b) Scenario-2: magnitude of ϕ_3 greater than the magnitude of ϕ_2. (c) T-model of the ILX structure.

detailed reluctance model for the ILX structure and how to derive essential electrical parameters. Section IV shows the design methodology and sensitivity analysis using FEM. Section V presents an analytical comparison of discrete structures and ILX structure, while Section VI shows their experimental validation under identical thermal conditions and operating points. Finally, Section VII concludes this article.

II. Operation of ILX Structure for DAB Converter

The proposed ILX structure uses off-the-shelf E-cores, as shown in Fig. 1(a). Here, the inductor section, consisting of E-cores with a prefixed gap in the middle limb, is placed on the top side of the transformer section. The transformer section consists of a gapless EE core arrangement. ILX structure comprises separate windings for the inductor and transformer, and their connections and sense of windings are shown in Fig. 1(b). The inductor winding, winding-1, is wound on the middle limb and is connected in series with the transformer's primary winding, winding-2. The transformer's secondary side winding is denoted by winding-3. Winding-1 and winding-3 are wound in a clockwise direction, whereas winding-2 is wound in a counterclockwise direction. In the ILX structure, transformer windings are wound concentrically, ensuring tight coupling. Winding-1, winding-2, and winding-3 produce the fluxes ϕ_1, ϕ_2, and ϕ_3, respectively. Inductor flux ϕ_1 is largely decoupled from the transformer fluxes ϕ_2 and ϕ_3. The presence of an airgap length l_g further ensures weak coupling. The airgap also allows the inductor to operate at higher values of winding current without saturation, and provides precise control of the inductance.

A. Superposition of Inductor and Transformer Fluxes in ILX Core

Fig. 2(a) and (b) shows the flux path for inductor flux ϕ_{ind} and transformer flux ϕ_{tx}. ϕ_{ind} is the same as ϕ_1 produced by winding-1. Whereas ϕ_{tx} is the combination of flux ϕ_2 and ϕ_3 produced by winding-2 and winding-3, respectively, and is given by $\phi_{\text{tx}} = \phi_2 - \phi_3$. The magnetizing component of the DAB transformer with the finite magnetizing inductance can alter the magnitude of I_p and I_s at the switching instants [17]. This change in current magnitude at the switching instance affects the magnitude of fluxes ϕ_2 and ϕ_3. The relation of these currents, which lead to scenario-1 and scenario-2, is given by (1). In (1), n_e represents the effective turns ratio of the ILX transformer

$$\begin{aligned} I_p > n_e I_s &\longrightarrow \phi_2 > \phi_3 \longrightarrow \text{Scenario-1} \\ I_p < n_e I_s &\longrightarrow \phi_2 < \phi_3 \longrightarrow \text{Scenario-2}. \end{aligned} \tag{1}$$

The main flux path (solid lines) and weakly coupled paths (dashed lines) of ϕ_{ind} and ϕ_{tx} for both scenario-1 and scenario-2 are highlighted in Fig. 2(a) and (b), respectively. The flux interaction in the shared core region becomes important as this region carries the main flux paths of both ϕ_{ind} and ϕ_{tx} fluxes. To analyze flux behavior in this region, it is imperative to calculate the magnitude of primary side currents I_p and secondary side currents I_s at the switching instants when finite magnetizing inductance is present. Fig. 2(c) illustrates the T-model of the ILX structure, which includes the magnetizing inductance L_m, series inductor L_e, and effective turns ratio n_e used to derive winding currents. In this model, V_{gm} and V_{om} represent the input and output voltages across the magnetic structure, respectively.

I_{1p} is the primary side current at switching instant $\frac{DT_s}{2}$ given by (2), I_{2p} is the primary side current at switching instant $\frac{T_s}{2}$ given by (3). Similarly, I_{1s} is the secondary side current at switching instant $\frac{DT_s}{2}$ given by (4) and I_{2s} is the secondary side current at switching instant $\frac{T_s}{2}$ given by (5). In these equations, M is the voltage ratio $(V_{om}/n_e V_{gm})$. T_s is the switching cycle time and D is the duty ratio

$$I_{1p} = \left[2DL_m + L_m(M-1)\right]\frac{V_{gm}T_s}{4L_eL_m} \tag{2}$$

$$I_{2p} = \left[L_m + ML_m(2D-1)\right]\frac{V_{gm}T_s}{4L_eL_m} \tag{3}$$

$$I_{1s} = \left[L_m(2D-1) + M(L_m+L_e)\right]\frac{V_{gm}T_s}{n_e 4L_eL_m} \tag{4}$$

Authorized licensed use limited to: TU Delft Library. Downloaded on April 14,2026 at 08:54:41 UTC from IEEE Xplore. Restrictions apply.

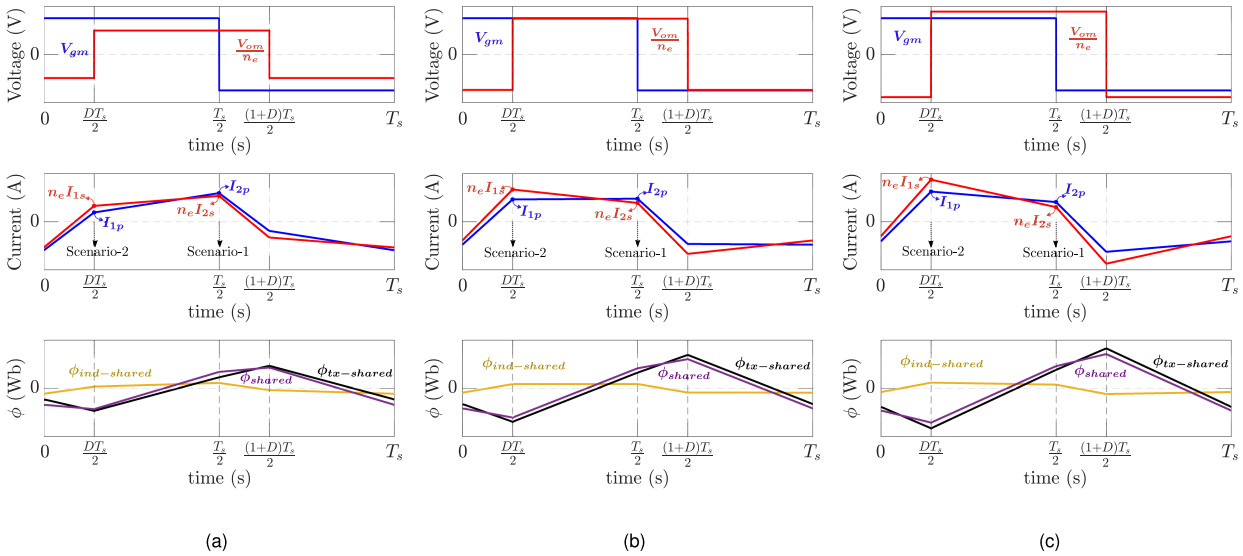

Fig. 3. DAB currents at switching instant and flux waveforms in the shared core segment for high load conditions when (a) voltage ratio M less than unity, (b) voltage ratio M equal to unity, and (c) voltage ratio M greater than unity.

$$I_{2s} = \left[M(L_m + L_e)(2D-1) + L_m\right]\frac{V_{gm}T_s}{n_e 4 L_e L_m}. \quad (5)$$

Fig. 3 shows the DAB switching waveforms based on (2)–(5) and highlights the behavior of the fluxes in the shared core segment at different switching instants. For all the cases shown, the output current is constant, and the value of M varies. It is observed that the magnitude of I_{1p} is smaller than n_eI_{1s} at switching instant $\frac{DT_s}{2}$ and magnitude of I_{2p} is higher than n_eI_{2s} at switching instant $\frac{T_s}{2}$. This results in the scenario-2 occurring at the instant $\frac{DT_s}{2}$ and the scenario-1 occurring at switching instant $\frac{T_s}{2}$.

Fluxes $\phi_{\text{ind-shared}}$ and $\phi_{\text{tx-shared}}$ are inductor and transformer fluxes in the shared core segment of ILX plotted separately, and ϕ_{shared} is the superposition of these two fluxes. Similar to the previous observation, at instance $\frac{DT_s}{2}$, $\phi_{\text{ind-shared}}$ and $\phi_{\text{tx-shared}}$ have opposite polarity (scenario-2) causing reduction in the magnitude of ϕ_{shared}. Whereas, for instance, $\frac{T_s}{2}$, $\phi_{\text{ind-shared}}$, and $\phi_{\text{tx-shared}}$ have the same polarity (scenario-1) causing increase in the magnitude of the ϕ_{shared}. This behavior effectively reduces the peak-to-peak magnitude of ϕ_{shared} in the ILX shared core segment, resulting in reduced core losses. This effect of reduction in peak-to-peak flux swing in the shared core segment increases as the $\phi_{\text{ind-shared}}$ increases in magnitude. Therefore, a higher reduction in core losses can be observed at the higher load current and higher power region.

III. Analytical Modeling of ILX Structure

This section first presents a detailed reluctance model based on flux paths. Subsequently, a simpler lumped-element magnetic circuit model is used to analyze ILX parameters. This analysis aims to derive permeance to calculate the self-inductance and mutual inductance of each winding. Once these parameters are obtained, a three-port coupled inductor model is then constructed, and electrical parameters such as the effective turns ratio, series inductance, and magnetizing inductance are then derived from the model.

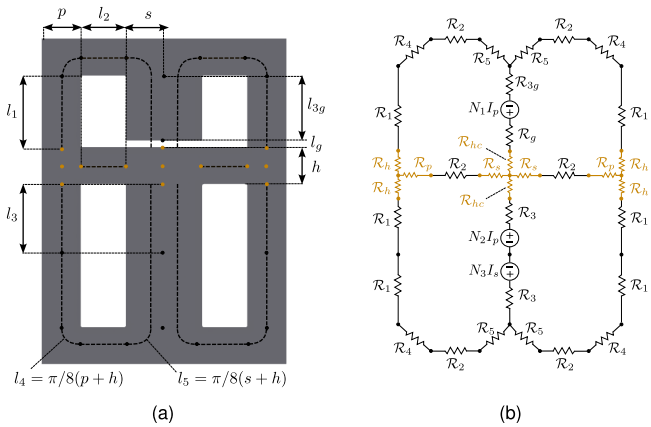

Fig. 4. (a) ILX core length dimensions. (b) ILX detailed reluctance model.

A. Detailed Reluctance Model of ILX Structure

The reluctance modeling in this work is carried out using ferrite cores, which exhibit isotropic properties and are thus well suited for the E-core stacking in ILX structures. A detailed reluctance model for the ILX structure is constructed based on the core's geometry, as shown in Fig. 4. Even though for both the inductor section and transformer section, the mean length of the flux paths and associated mean area can be obtained according to the IEC 60 205 standard, calculating the mean parameters for the shared core segment is challenging. This is primarily because the flux at the junction splits into two paths, making it difficult to estimate the reluctance of these junctions, as the path occupied by these fluxes can change significantly with operating conditions.

Authorized licensed use limited to: TU Delft Library. Downloaded on April 14,2026 at 08:54:41 UTC from IEEE Xplore. Restrictions apply.

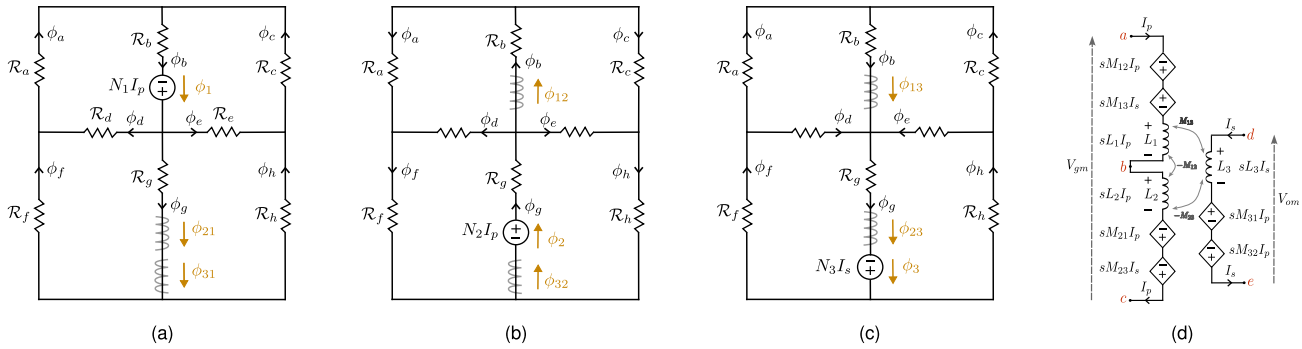

Fig. 5. (a) Flux components due to winding-1. (b) Flux components due to winding-2. (c) Flux components due to winding-3. (d) Three-port coupled inductor model of the ILX magnetic structure.

TABLE II
ILX RELUCTANCES

Reluctance	Reluctance	Cross-section Area
$\mathcal{R}_1 = \frac{l_1}{\mu_0\mu_r A_1}$	$\mathcal{R}_5 = \frac{l_5}{\mu_0\mu_r A_5}$	$A_1 = pw$
$\mathcal{R}_2 = \frac{l_2}{\mu_0\mu_r A_2}$	$\mathcal{R}_h = \frac{h/2}{\mu_0\mu_r A_1}$	$A_2 = hw$
$\mathcal{R}_3 = \frac{l_3}{\mu_0\mu_r 2A_3}$	$\mathcal{R}_p = \frac{p/2}{\mu_0\mu_r A_2}$	$A_3 = sw$
$\mathcal{R}_{3g} = \frac{l_{3g}}{\mu_0\mu_r 2A_3}$	$\mathcal{R}_s = \frac{s}{\mu_0\mu_r A_2}$	$A_4 = \frac{A1+A2}{2}$
$\mathcal{R}_4 = \frac{l_4}{\mu_0\mu_r A_4}$	$\mathcal{R}_{hc} = \frac{h/2}{\mu_0\mu_r 2A_3}$	$A_5 = \frac{A2+A3}{2}$

Therefore, the fluxes in these junctions are approximated by considering the reluctance $\mathcal{R}_h$, $\mathcal{R}_p$, $\mathcal{R}_s$, and $\mathcal{R}_{hc}$. Reluctance of the airgap R_g, is obtained using the 3-D airgap reluctance calculation method, as described in [18], which leads to accurate modeling of fringing effects. All the other reluctances are defined, as shown in Table II, where the depth of the core is given by w.

B. Three-Port Coupled Inductor Model of ILX Structure

Fig. 5 shows the simplified lumped reluctance model for the ILX structure, obtained by combining the reluctance in each branch of the detailed model. The fluxes in each branch are determined by solving four equations with four unknowns in the presence of one MMF source at a time. Fig. 5(a)–(c) shows the flux components produced by winding-1 ($\phi_1, \phi_{21},$ and ϕ_{31}), winding-2 ($\phi_2, \phi_{12},$ and ϕ_{32}), and winding-3 ($\phi_3, \phi_{13},$ and ϕ_{23}), respectively. The permeance of space occupied by these fluxes can be derived, as shown in Table III. The self-inductance and mutual inductance of ILX windings are then calculated using these permeances. The three-port coupled inductor model of the ILX magnetic structure is constructed by using an inductor for the self-inductance and dependent voltage sources for the coupling term, as shown in Fig. 5(d).

C. Derivation of DAB Converter Essential Electrical Parameters

The essential electrical parameters $n_e, L_e,$ and L_m are directly obtained from the inductance matrix of the ILX structure, extracted using the configuration shown in Fig. 5(d). The leakage associated with the transformer section of the ILX is assumed to be negligible, and reciprocity is enforced such that $M_{12} = M_{21}$, $M_{13} = M_{31}$, and $M_{23} = M_{32}$. Applying KVL in Fig. 5(d), the obtained inductance matrix is shown in

$$\begin{bmatrix} L_1 + L_2 - 2M_{12} & M_{23} - M_{13} \\ M_{23} - M_{13} & L_3 \end{bmatrix}. \tag{6}$$

The effective turns ratio n_e is obtained using (6) and is expressed in

$$n_e = \frac{L_3}{M_{23} - M_{13}}. \tag{7}$$

Using this result, the series inductance can be derived from (6) and is given by

$$L_e = L_1 - M_{12} + \frac{M_{13}}{n_e} \tag{8}$$

where M_{12} and $\frac{M_{13}}{n_e}$ are equal in magnitude, leading to series inductance determined by the L_1 term. Following the same approach, the magnetizing inductance L_m is also obtained from (6) and is expressed in

$$L_m = L_2 - M_{12} - \frac{M_{13}}{n_e}. \tag{9}$$

Because the contributions of the coupling terms M_{21} and $\frac{M_{13}}{n_e}$ are negligible, L_m is effectively determined by the self-inductance L_2.

IV. DESIGN OF ILX FOR DAB

The goal of the ILX design is to reduce the flux swing by utilizing the flux superposition concept and ensuring that the flux density in any region of the core is below the maximum flux density B_m. The design for ILX is based on an analytical model for quick iterations. It consists of selecting the correct sense of winding, the number of turns for each winding, core size, and litz-wire dimensions to meet the DAB converter specification outlined in Table IV. The gap length is prefixed for the off-the-shelf cores and is not optimized in this design.

A. Sense of Winding

The sense of winding determines the orientation of the fluxes of each winding. A clockwise direction for winding-1 and winding-3 and a counterclockwise direction for winding-2 is

Authorized licensed use limited to: TU Delft Library. Downloaded on April 14,2026 at 08:54:41 UTC from IEEE Xplore. Restrictions apply.

TABLE III
PERMEANCES OF FLUXES PRODUCED IN ILX STRUCTURE

Permeance	Values	Permeance	Values	Permeance	Values
$\mathcal{P}_{b1}$, $\mathcal{P}_1$	$\frac{\phi_b}{N_1 I_p} = \frac{\phi_1}{N_1 I_p}$	$\mathcal{P}_{b2}$, $\mathcal{P}_{12}$	$\frac{\phi_b}{N_2 I_p} = \frac{\phi_{12}}{N_2 I_p}$	$\mathcal{P}_{b3}$, $\mathcal{P}_{13}$	$\frac{\phi_b}{N_3 I_s} = \frac{\phi_{13}}{N_3 I_s}$
$\mathcal{P}_{g1}$, $\mathcal{P}_{21}$, $\mathcal{P}_{31}$	$\frac{\phi_g}{N_1 I_p} = \frac{\phi_{21}}{N_1 I_p} = \frac{\phi_{31}}{N_1 I_p}$	$\mathcal{P}_{g2}$, $\mathcal{P}_2$, $\mathcal{P}_{32}$	$\frac{\phi_g}{N_2 I_p} = \frac{\phi_2}{N_2 I_p} = \frac{\phi_{32}}{N_2 I_p}$	$\mathcal{P}_{g3}$, $\mathcal{P}_{23}$, $\mathcal{P}_3$	$\frac{\phi_g}{N_3 I_s} = \frac{\phi_{23}}{N_3 I_s} = \frac{\phi_3}{N_3 I_s}$
$\mathcal{P}_{a1}$	$\phi_a / N_1 I_p$	$\mathcal{P}_{a2}$	$\phi_a / N_2 I_p$	$\mathcal{P}_{a3}$	$\phi_a / N_3 I_s$
$\mathcal{P}_{c1}$	$\phi_c / N_1 I_p$	$\mathcal{P}_{c2}$	$\phi_c / N_2 I_p$	$\mathcal{P}_{c3}$	$\phi_c / N_3 I_s$
$\mathcal{P}_{d1}$	$\phi_d / N_1 I_p$	$\mathcal{P}_{d2}$	$\phi_d / N_2 I_p$	$\mathcal{P}_{d3}$	$\phi_d / N_3 I_s$
$\mathcal{P}_{e1}$	$\phi_e / N_1 I_p$	$\mathcal{P}_{e2}$	$\phi_e / N_2 I_p$	$\mathcal{P}_{e3}$	$\phi_e / N_3 I_s$
$\mathcal{P}_{f1}$	$\phi_f / N_1 I_p$	$\mathcal{P}_{f2}$	$\phi_f / N_2 I_p$	$\mathcal{P}_{f3}$	$\phi_f / N_3 I_s$
$\mathcal{P}_{h1}$	$\phi_h / N_1 I_p$	$\mathcal{P}_{h2}$	$\phi_h / N_2 I_p$	$\mathcal{P}_{h3}$	$\phi_h / N_3 I_s$

TABLE IV
DAB CONVERTER SPECIFICATION

	Parameters	Values
DAB converter	Input voltage V_g	775 V
	Output voltage $V_{o-\min}$-$V_{o-\max}$	250–450 V
	Max. output current $I_{o-\max}$	28 A
	Max. rms primary $I_{p-\mathrm{rms}-\max}$	17 A
	Max. rms secondary $I_{s-\mathrm{rms}-\max}$	34 A
	Max. output power $P_{o-\max}$	11 kW
	Operating frequency f_s	50 kHz
	Series inductor L_e	103 μH
	Magnetizing inductor L_m	High (not controlled)
	Turns ratio n	0.5
Magnetics	Max. flux density B_m,	0.2 T
	Window packaging factor k_w	0.25
	Max. current density J_m	3 A/mm^2
	Apparent power VA	15 kVA

chosen to allow flux reduction (scenario-2) to happen at instance $\frac{DT_s}{2}$. This reduces the peak-to-peak flux magnitude in the shared core segment as the inductor current scales up in the high-power operating region.

B. Iterative Design Method for the ILX Structure

Integrating a DAB power inductor, which consists of large high-frequency current ripples, with a DAB transformer on the same core poses design challenges. Standard methods, such as the areas-product A_p or core geometry k_g approach, cannot be applied directly. Therefore, an iterative design approach is chosen, and sizing of the ILX is carried out, considering maximum flux density B_m as a limiting constraint. It is essential to note that B_m is the design variable, not the saturation limit of the core material. The design is done to meet the series inductor L_e and turns ratio n requirement. Fig. 6 shows the design flow for the ILX structure. The design flow begins by choosing EE-cores for the transformer section based on the area product approach. For the given parameters, such as volt–amp VA rating, maximum flux density B_m, operating frequency f_s, maximum current density J_m, and a window utilization factor k_w, the area product A_p is given by [17]

$$A_p = \frac{\mathrm{VA}}{2 f_s k_w J_m B_m}. \tag{10}$$

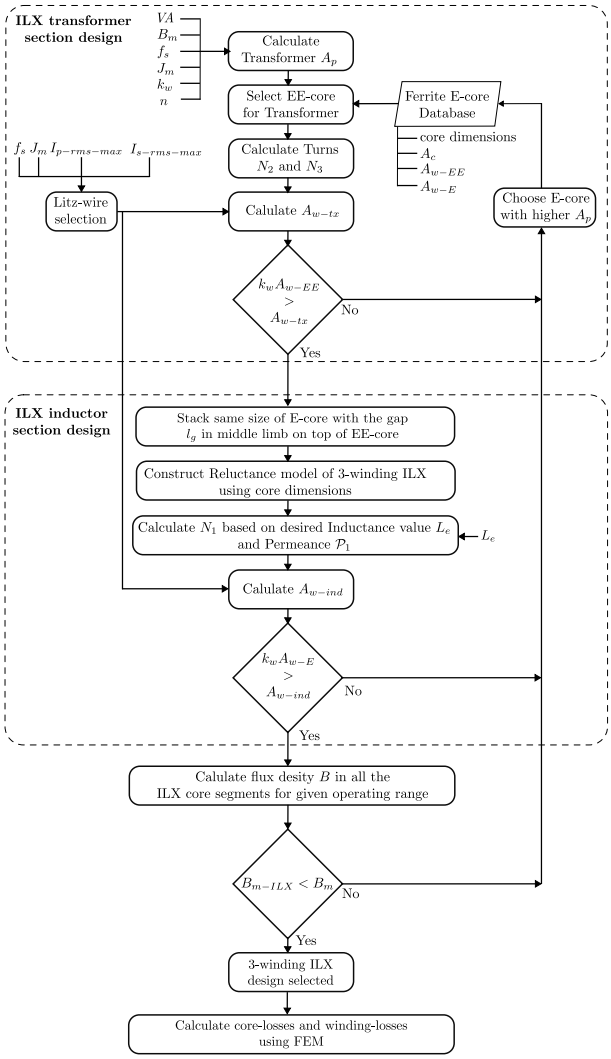

Fig. 6. Iterative design flow for ILX structure.

An appropriate EE-core size is chosen from the database with A_p higher than the calculated area product. Based on the core dimensions and DAB converter specifications, turns N_2 and N_3 are calculated using [17]

$$N_3 = \frac{V_{o-\mathrm{avg}}}{4 A_c B_m f_s} \qquad N_2 = N_3 / n \tag{11}$$

Authorized licensed use limited to: TU Delft Library. Downloaded on April 14,2026 at 08:54:41 UTC from IEEE Xplore. Restrictions apply.

where $V_{o-\text{avg}}$ is a half-cycle average of maximum output voltage, and A_c is the core cross-section area. N_2 and N_3 are rounded off to the nearest higher integer. Litz wires are used for the ILX windings, and the number of strands n_s, strand diameter d_s, and conductor cross-section area A_{litz} are selected based on the maximum current density J_m and the skin depth criteria. $A_{w-\text{tx}}$ is the combined cross-section area of the selected litz wire winding for N_p and N_s turns. The chosen EE-core for the transformer is qualified if the product of the window area of EE-core $A_{w-\text{EE}}$ and the window packaging factor k_w is greater than $A_{w-\text{tx}}$. Otherwise, a core with a larger A_p is chosen until it meets this criterion.

The next step in the design process is to place the same size E-core with the prefixed airgap l_g in the middle limb on the top side of the EE-core and construct the reluctance network model, as shown in Fig. 4(b), based on the core dimensions. Once the reluctance model is constructed, permeance $\mathcal{P}_1$ can be extracted by the method outlined in Section III. The number of turns N_1 required for series inductance L_e can be obtained from

$$N_1 = \sqrt{\frac{L_1}{\mathcal{P}_1}} \quad \text{where} \quad L_1 = L_e + M_{12} - \frac{M_{13}}{n_e}. \tag{12}$$

The cross-sectional area of the inductor winding for N_1 turns is given by $A_{w-\text{ind}}$. If the product of the window area of E-core A_{w-E} and the window packaging factor k_w is greater than $A_{w-\text{ind}}$, the design is qualified. Otherwise, an E-core with a higher A_p is chosen, as shown in Fig. 6.

Once the inductor section design is done, the flux densities of all the segments of ILX core are calculated using (13), and the maximum among them $B_{m-\text{ILX}}$, given by (14), is compared with B_m. In these equations, $A_{c-a}, A_{c-b} \ldots A_{c-h}$ are the cross-sectional areas of segments $a, b \ldots h$, respectively. If $B_{m-\text{ILX}}$ is lower than B_m, the design is selected, or else the core with higher A_p is chosen, and the ILX design is re-iterated. The final step is the loss evaluation using a finite element model (FEM). ILX core is modeled in COMSOL, and a 2-D magnetostatic simulation is used to obtain B-field and H-field to evaluate the core and winding losses. This design step aims to validate the design at a high-power operating point

$$\begin{aligned}
B_a &= (I_p N_1 \mathcal{P}_{a1} - I_p N_2 \mathcal{P}_{a2} + I_s N_3 \mathcal{P}_{a3})/A_{c-a} \\
B_b &= (I_p N_1 \mathcal{P}_{b1} - I_p N_2 \mathcal{P}_{b2} + I_s N_3 \mathcal{P}_{13})/A_{c-b} \\
B_c &= (I_p N_1 \mathcal{P}_{c1} - I_p N_2 \mathcal{P}_{c2} + I_s N_3 \mathcal{P}_{c3})/A_{c-c} \\
B_d &= (I_p N_1 \mathcal{P}_{d1} + I_p N_2 \mathcal{P}_{d2} - I_s N_3 \mathcal{P}_{d3})/A_{c-d} \\
B_e &= (I_p N_1 \mathcal{P}_{e1} + I_p N_2 \mathcal{P}_{e2} - I_s N_3 \mathcal{P}_{e3})/A_{c-e} \\
B_f &= (I_p N_1 \mathcal{P}_{f1} - I_p N_2 \mathcal{P}_{f2} + I_s N_3 \mathcal{P}_{f3})/A_{c-f} \\
B_g &= (I_p N_1 \mathcal{P}_{g1} - I_p N_2 \mathcal{P}_{g2} + I_s N_3 \mathcal{P}_{g3})/A_{c-g} \\
B_h &= (I_p N_1 \mathcal{P}_{h1} - I_p N_2 \mathcal{P}_{h2} + I_s N_3 \mathcal{P}_{h3})/A_{c-h}
\end{aligned} \tag{13}$$

$$B_{m-\text{ILX}} = \max(B_a, B_b, B_c, B_d, B_e, B_f, B_g, B_h). \tag{14}$$

V. Design Verification and Analytical Evaluation

The ILX structure is designed as per the iterative design methodology presented in Section IV, and the design parameters and outcomes are summarized in Table V. Fig. 7 shows the magnetic flux distribution of the ILX structure operated at a maximum power of 11 kW and an output voltage of 450 V using 2-D-magnetostatic FEM simulation. It is observed that the flux density distribution is symmetric across the vertical axis, showing the same distribution on both halves of the core, as compared to [11], which leads to improved core utilization.

TABLE V
Design Inputs and Outcomes for Discrete and ILX Structures

Parameters	Discrete inductor	Discrete transformer	ILX structure
B_m	0.2 T	0.2 T	0.2 T
Core	N27 E70-33-32 2xEE	N27 E70-33-32 4xEE	N27 E70-33-32 4xEE(Tx), 4xE(L)
Airgap	1.5 mm	0	1.5 mm
Litz wire	n_s = 200, d_s = 0.2 mm, A_{litz} = 12.2 mm^2	n_s = 200, d_s = 0.2 mm, A_{litz} = 12.2 mm,^{2} 1L/1L parallel	n_s = 200, d_s = 0.2 mm, A_{litz} = 12.2 mm,^{2} 1L/1L parallel
Turns	9	8:4	6:8:4
Volume	223 170 cm^3	450 560 cm^3	671 620 cm^3
Winding length	1.791 m	3.924 m	5.886 m
L_e	**(FEM)** 102.6 μH	NA	**(FEM)** 102.95 μH **(Analytical)** 103.39 μH
L_m	NA	**(FEM)** 2.418 mH	**(FEM)** 2.399 mH **(Analytical)** 2.067 mH

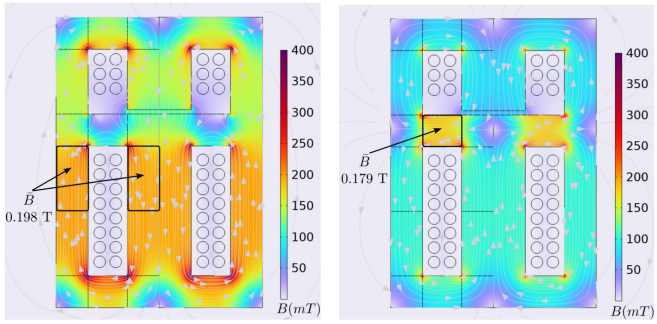

Fig. 7. ILX magnetic flux distribution operated at 11 kW and 450 V, shown at switching instant of (a) $\frac{DT_s}{2}$ and (b) $\frac{T_s}{2}$.

The ILX core is segmented to evaluate the average flux density $\bar{B}$ of each segment. For switching instant $\frac{DT_s}{2}$, the maximum value of $\bar{B}$, 0.198 T occurs in transformer section and for switching instant $\frac{T_s}{2}$, the maximum value of $\bar{B}$, 0.179 T occurs in the shared core segment.

A. Airgap Sensitivity Analysis for ILX Structure

An airgap sensitivity analysis is carried out to validate that the ILX structure can allow independent tuning of series inductance without reducing the magnetizing inductance. From Fig. 8, it is observed that the value of L_e can be independently tuned by varying the gap length l_g for the fixed number of inductor turns

Authorized licensed use limited to: TU Delft Library. Downloaded on April 14,2026 at 08:54:41 UTC from IEEE Xplore. Restrictions apply.

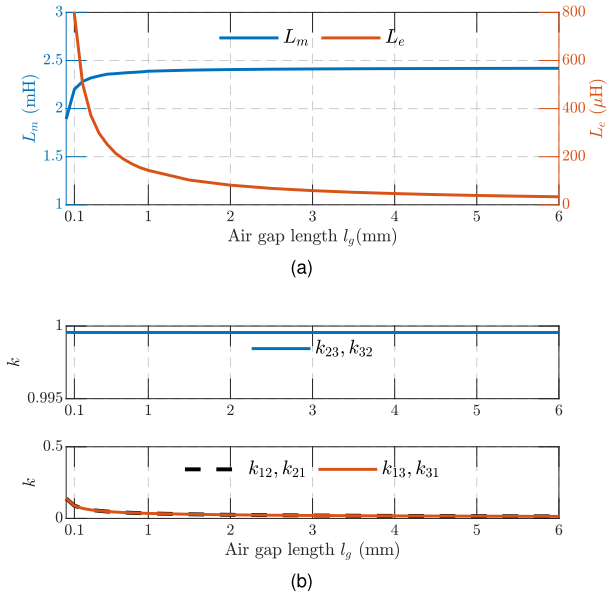

Fig. 8. Effect of airgap variation on (a) magnetizing and series inductance and (b) coupling coefficients.

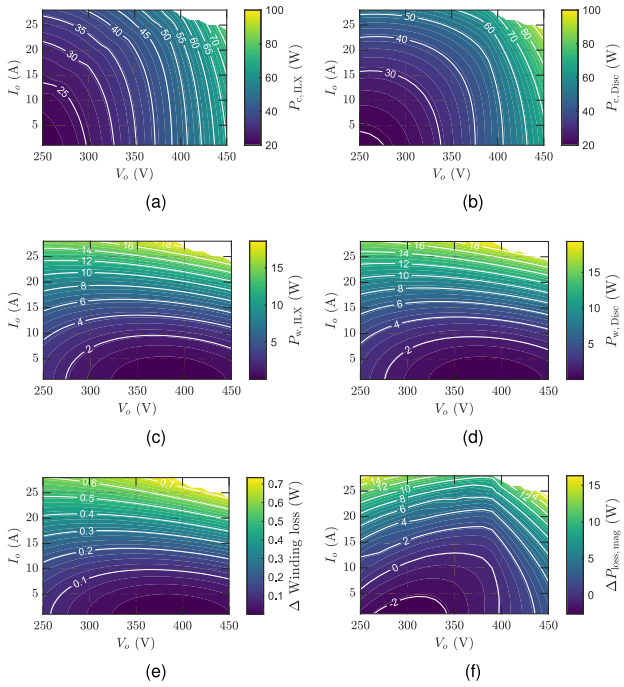

Fig. 9. (a) Core loss of ILX structure, $P_{\mathrm{c,\,ILX}}$. (b) Core loss of discrete structures, $P_{\mathrm{c,\,Disc}}$. (c) Winding loss of ILX structure, $P_{\mathrm{w,\,ILX}}$. (d) Winding loss of discrete structures, $P_{\mathrm{w,\,Disc}}$. (e) Difference in winding losses, ($P_{\mathrm{w,\,Disc}} - P_{\mathrm{w,\,ILX}}$). (f) Difference in magnetic losses, ($P_{\mathrm{loss,\,Disc}} - P_{\mathrm{loss,\,ILX}}$).

N_1. But for zero gap length, the coupling coefficient between the inductor winding and transformer winding (k_{12}, k_{21}, k_{13}, and k_{31}) is around 0.13, causing a slight reduction (10%) in the value of L_m. However, the ILX core with a zero airgap length can result in core saturation and is not practical. For the selected ILX cores with $N_1 = 6$ turns, it is analytically obtained that a minimum airgap length of 1.34 mm is required to keep the maximum flux density below 0.2 T while meeting the L_e design target. In ILX, the off-the-shelf prefixed gapped cores are used in the inductor section, which creates weak coupling between ϕ_{tx} and ϕ_{ind} and allows higher current saturation limits. Furthermore, the value of L_e can also be tuned by N_1 turns, as shown in Section IV. For the given design, employing a 1.5 mm l_g, the L_m is not reduced, and the coupling coefficient between the inductor and transformer windings is 0.02, which indicates weak coupling. In addition, it can be inferred from k_{23} and k_{32} that the coupling between transformer primary and secondary windings is close to unity, and therefore, the leakage inductance expected is very minimal.

B. Discrete and ILX Structure Loss Comparison

FEM derived design parameters of the discrete transformer, discrete inductor, and ILX structure listed in Table V are used for loss calculations. Core loss and winding loss for all structures are evaluated with the help of FEM simulation. Assumptions such as the constant and uniform core temperature of 90 °C and winding temperature of 100 °C are considered for loss calculations. The discrete and ILX structures use identical Litz wire. In both the discrete transformer and ILX designs, the primary winding consists of a single layer, while the secondary employs a single layer of parallel windings. The following conditions are considered to ensure a fair comparison between ILX and discrete structures.

1) ILX, discrete inductor, and transformer are designed with the same maximum flux density B_m of 0.2 T.
2) The combined volume of the discrete inductor and transformer is almost the same as the volume of the ILX structure.
3) The combined length of winding used in the discrete inductor and transformer is close to the length of windings used in the ILX structure.
4) The series inductance and magnetizing inductance of discrete and ILX structures obtained from FEM are within a 1% margin.

Fig. 9(a) and (b) shows the FEM-based absolute core loss calculations for ILX, $P_{\mathrm{c,\,ILX}}$, and the combined discrete structures, $P_{\mathrm{c,\,Disc}}$, respectively. Similarly, Fig. 9(c) and (d) shows the FEM based absolute winding loss calculations for ILX, $P_{\mathrm{w,\,ILX}}$, and the combined discrete structures, $P_{\mathrm{w,\,Disc}}$, respectively. Fig. 9(e) shows the difference in winding loss obtained by subtracting the ILX structure's winding loss $P_{\mathrm{w,\,ILX}}$ from the total winding loss of the discrete inductor and transformer, $P_{\mathrm{w,\,Disc}}$. It is observed that the range of delta winding loss is very small across the region, indicating that the winding loss can be considered more or less equal for both the ILX and combined discrete structures. Furthermore, Fig. 9(f) shows the $\Delta P_{\mathrm{loss,\,mag}}$, which is the difference in total loss in the discrete structures, $P_{\mathrm{loss,\,Disc}}$ and ILX structure, $P_{\mathrm{loss,\,ILX}}$ ($\Delta P_{\mathrm{loss,\,mag}} = P_{\mathrm{loss,\,Disc}} - P_{\mathrm{loss,\,ILX}}$). It is observed that $\Delta P_{\mathrm{loss,\,mag}}$ is significant at the high power region, indicating that the ILX structure reduces the losses. This reduction in losses is due to the phenomenon explained in Section II-A, where the peak-to-peak flux swing ϕ_{shared} is

Authorized licensed use limited to: TU Delft Library. Downloaded on April 14,2026 at 08:54:41 UTC from IEEE Xplore. Restrictions apply.

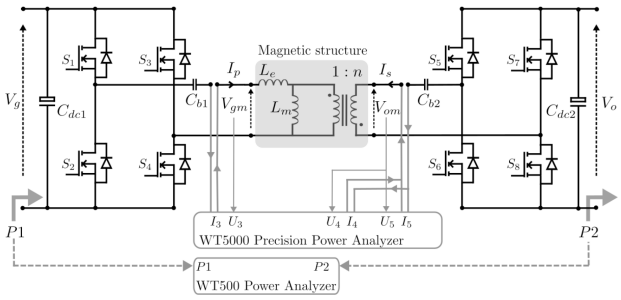

Fig. 10. Electrical connection of the magnetic structure test setup.

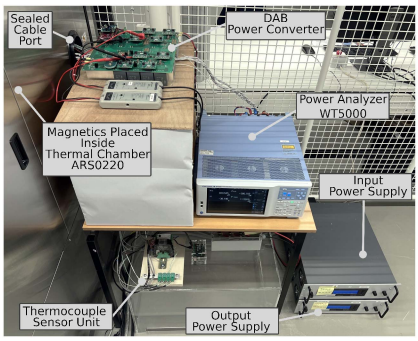

Fig. 11. Layout of the experiment setup.

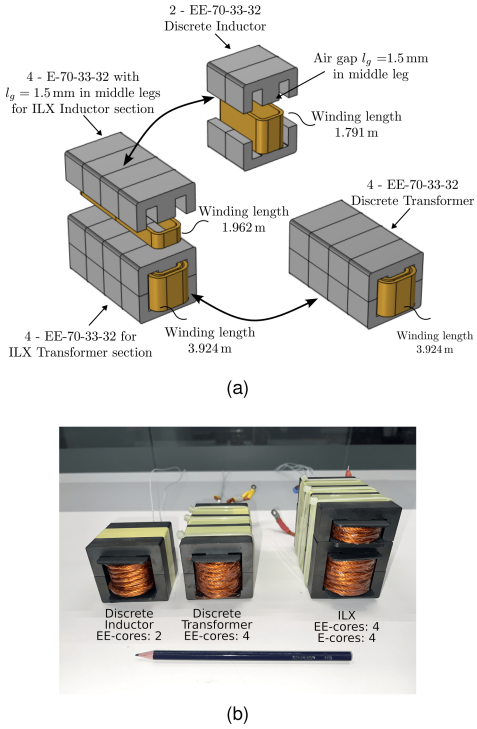

Fig. 12. Comparison of discrete and ILX structures using (a) 3-D visualization of their physical parts and (b) actual images used in the experiments.

reduced in the shared region of the core due to the presence of opposing inductor and transformer flux.

VI. Experimental Results

This section shows the experimental setup and results to validate the high power efficiency benefits of an ILX structure compared to a combined discrete structure for a DAB converter.

A. Experimental Setup

Figs. 10 and 11 show the electrical connections and actual layout of the experiment setup. Switches S_1 to S_8 generate phase-shifted excitation voltages for the selected magnetic configuration. C_{dc1} are C_{dc2} are dc-bus capacitors, whereas C_{b1} and C_{b2} are dc-blocking capacitors. V_g and V_o are the input and the output voltages of DAB converter, respectively. The magnetic losses are measured using a YOKOGAWA WT5000 precision power analyzer. The magnetic structure's input voltage V_{gm} and current I_p are measured by channel-3. Whereas the output voltage V_{om} and current I_s of the magnetic structure are measured by paralleling channel-4 and channel-5. This parallel arrangement is done to avoid exceeding the current limit of the power analyzer. For each comparative test, the output voltage V_o and the output power P_o of the power converter are kept constant. In addition, the ambient temperature is maintained with the help of the environmental test chamber ARS0220 throughout the test for a fair comparison. The minimum ambient temperature is kept at 4 °C. Power loss measurements using a power analyzer are made when the magnetic structures have attained a steady-state temperature, ensuring stable core and winding loss measurements. Experimental validation has been carried out up to 9 kW, below the 11 kW converter rating, as thermal limitations in the magnetic structures prevented reliable testing at higher power. Furthermore, the overall DAB converter efficiency is evaluated using a YOKOGAWA WT500 power analyzer by measuring the converter's input and output port powers, P1 and P2, respectively, to study the impact of the ILX structure with respect to discrete structures.

B. Physical Construction and Measured Electrical Parameters of Both Magnetic Structures

Fig. 12(a) shows the 3-D visualization of the ILX and discrete structures, and Fig. 12(b) shows the actual parts placed side-by-side. It can be observed that the total number of E-cores is the same in the combined discrete structure and the ILX structure. Thermocouples are used to sense the worst-case temperature and to identify the thermal equilibrium state of each magnetic structure. The thermocouples are mounted on the center limb of the core and in the center region of the winding to measure the worst-case core and winding temperatures.

Both discrete and ILX structures are constructed based on the parameters outlined in Table V. The electrical parameters of these structures are measured using a KEYSIGHT E4990 A impedance analyzer and are listed in Table VI. In the ILX structure, L_1, L_2, and L_3 denote the self-inductances of the three windings. For comparison, the discrete inductor corresponds to L_1, while the discrete transformer windings correspond to L_2 (primary) and L_3 (secondary). Mutual inductances of the

Authorized licensed use limited to: TU Delft Library. Downloaded on April 14,2026 at 08:54:41 UTC from IEEE Xplore. Restrictions apply.

TABLE VI
EXPERIMENTALLY MEASURED ELECTRICAL PARAMETERS AND INSULATION CLASSES OF MAGNETIC STRUCTURES

	Parameter	Discrete inductor	Discrete transformer	ILX structure
Measured	L_1	104.51 μH	–	102.14 μH
	L_2	–	2.518 mH	2.517 mH
	L_3	–	638 μH	631 μH
	M_{12}, M_{21}	–	–	8.62 μH
	M_{13}, M_{31}	–	–	6.76 μH
	M_{23}, M_{32}	–	1.255 mH	1.237 mH
	Transformer leakage	–	3 μH	2.97 μH
Insulation	Litz wire	Class 200	Class 200	Class 200
	Coil former	Class F	PET-CF (205°C)	PET-CF (205°C)
	Polyimide tape	Class 220	Class 220	Class 220
	Polyester film tape	130°C	130°C	130°C
	Polyamide 46 tie	150°C	150°C	150°C

ILX structure are also measured to derive the coupling coefficient. The calculated coupling coefficient between the ILX inductor and transformer windings is close to zero, indicating weak coupling. In contrast, the coefficient between the ILX transformer's primary and secondary windings is near unity, reflecting strong coupling. The leakage inductance inferred on the primary side is measured for both the discrete transformer and the ILX transformer. The value of leakage is small in both structures compared to the value of L_e, and therefore its effect is neglected. The insulation class of the magnetic components is provided in Table VI. Polyimide tape is used for extra winding and interlayer insulation, while coil formers (PET-CF), polyester film tape, and polyamide 46 ties are employed for structural purposes. These materials do not have a specified insulation class but are rated by their maximum operating temperatures.

C. Comparative Test Measurements

Comparative tests are performed at different DAB converter output voltage V_o and output power P_o to benchmark the power loss of the ILX structure against the combined power loss of the discrete structures. For all tests, the input voltage is fixed at 775 V, and the ambient temperature is actively regulated by the thermal chamber to ensure consistent thermal conditions during continuous operation. Three representative operating points are evaluated in detail: a high-voltage, high-power case (450 V, 9 kW at 4 °C), a low-voltage, high-power case (250 V, 7 kW at 4 °C), and a mid-voltage, low-power case at typical room temperature (387.5 V, 3 kW at 25 °C). Furthermore, the DAB converter efficiency of both magnetic structures is compared.

Fig. 13 presents WT5000 power analyzer data for 450 V, 9 kW operating point. It is observed that the power loss dissipation in ILX, $P_{\text{loss, ILX}}$ is 150.1 W and the power loss in the discrete structures, $P_{\text{loss, Disc}}$ is 164.6 W. This represents an approximately 8.8% reduction in loss using the proposed ILX structure. The measured loss of each magnetic structure is subject to WT5000 measurement uncertainty, and therefore, the difference in total loss $\Delta P_{\text{loss, mag}}$ is used to evaluate the performance of the ILX structure. At 450 V, 9 kW operating point, $\Delta P_{\text{loss, mag}}$ is 14.5 W. The worst-case core and winding

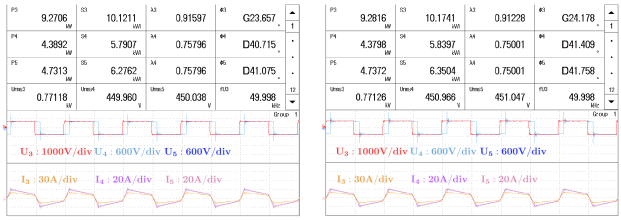

Fig. 13. WT5000 power analyzer data at 450 V, 9 kW, and 4 °C test condition for the (a) ILX structure and (b) discrete structures.

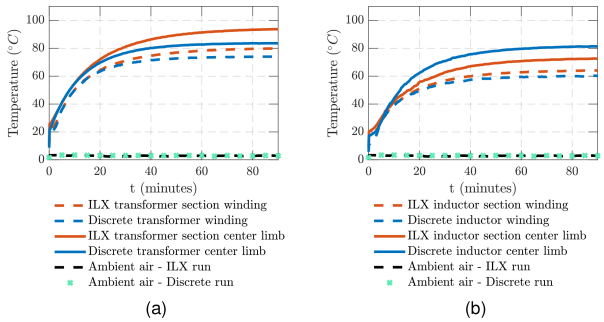

Fig. 14. Thermocouple data 450 V, 9 kW, and 4 °C test condition results for the (a) ILX transformer section and a discrete transformer and (b) ILX inductor section and a discrete inductor.

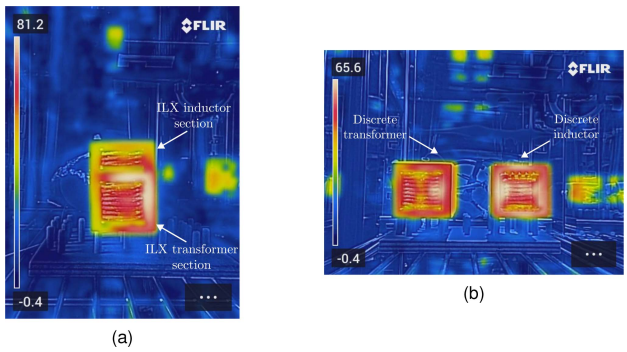

Fig. 15. Steady-state infrared thermal image at 450 V, 9 kW, and 4 °C test condition for the (a) ILX structure and (b) discrete structures.

temperatures of ILX and discrete structures measured using thermocouples are shown in Fig. 14. Both ILX and discrete structures reach steady-state temperature after 90 min of continuous operation. The worst-case core temperature of the ILX transformer section is 10.1 °C higher than that of the discrete transformer, whereas the worst-case core temperature of the discrete inductor is 8.1 °C higher than that of the ILX inductor section. Furthermore, Fig. 15 shows the steady-state thermal image of both magnetic structures captured inside the thermal chamber using the infrared thermal imaging camera FLIR C5. The ILX structure shows a nonuniform thermal distribution with hot spots on the transformer section and the shared core region, whereas both the discrete inductor and the discrete transformer exhibit a near-uniform thermal distribution, with hot spots visible in the middle region of the inductor core.

Authorized licensed use limited to: TU Delft Library. Downloaded on April 14,2026 at 08:54:41 UTC from IEEE Xplore. Restrictions apply.

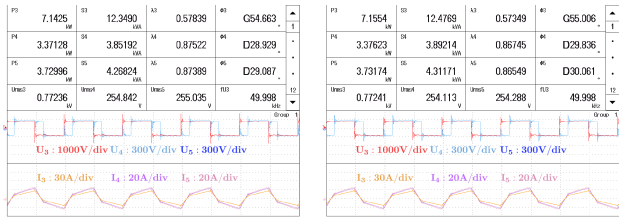

Fig. 16. WT5000 power analyzer data at 250 V, 7 kW, and 4 °C test condition for the (a) ILX structure and (b) discrete structures.

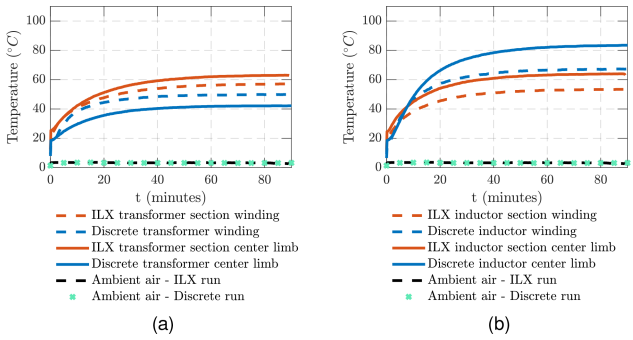

Fig. 17. Thermocouple data 250 V, 7 kW, and 4 °C test condition results for the (a) ILX transformer section and a discrete transformer and (b) ILX inductor section and a discrete inductor.

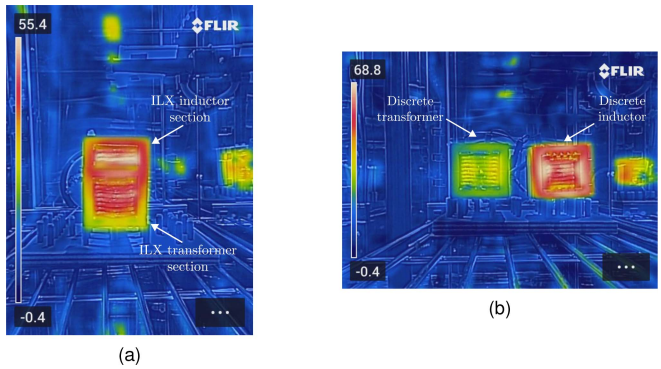

Fig. 18. Steady-state infrared thermal image at 250 V, 7 kW, and 4 °C test condition for the (a) ILX structure and (b) discrete structures.

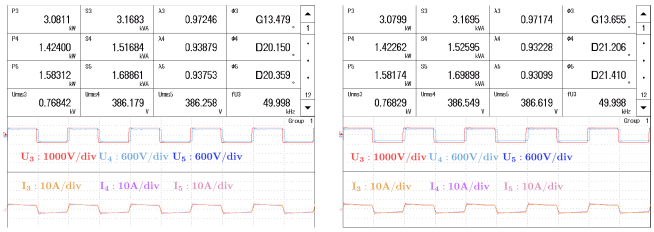

Fig. 19. WT5000 power analyzer data at 387.5 V, 3 kW, and 25 °C test condition for the (a) ILX structure and (b) discrete structures.

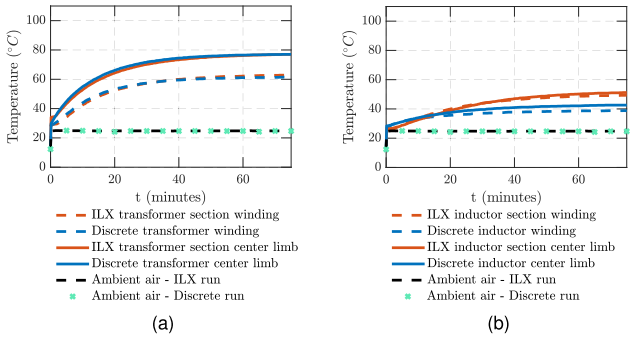

Fig. 20. Thermocouple data at 387.5 V, 3 kW, and 25 °C test condition results for the (a) ILX transformer section and a discrete transformer and (b) ILX inductor section and a discrete inductor.

Fig. 16 shows WT5000 power analyzer data for both ILX and discrete structures captured at 250 V, 7 kW operating point. It is observed that the power loss in ILX, $P_{\text{loss, ILX}}$ is 41.26 W and power loss in discrete structures is $P_{\text{loss, Disc}}$ is 47.43 W. This corresponds to a 13% loss reduction with the ILX structure, where $\Delta P_{\text{loss, mag}}$ is 6.17 W. This demonstrates that the ILX consistently achieves lower losses in the high-power region. Furthermore, Fig. 17 shows thermocouple measured data for ILX and discrete structures, the steady-state is achieved around 90 min of continuous operation, similar to 450 V, 9 kW operating point. The discrete inductor core reaches a maximum temperature of 83.5 °C, while the ILX inductor section core reaches 63.6 °C, showing a reduction of about 20 °C. In contrast, the discrete transformer core temperature is 42.2 °C, whereas the ILX transformer section core reaches 62.9 °C, an increase of about 20 °C. This thermal behavior is also evident in the thermal images of ILX and discrete structures, as shown in Fig. 18. The thermal coupling between the transformer and inductor sections in the ILX core reduces the temperature gradient between the hottest and coolest regions of the core. In contrast, the discrete structures exhibit a larger temperature difference between the individual components.

To evaluate the performance of the magnetic structures under a typical ambient temperature of 25 °C, an additional test is performed at 387.5 V output voltage and 3 kW output power. This operating point ensures that both the ILX and discrete structures operate within their thermal insulation limits. Fig. 19 presents the WT5000 power analyzer data for the ILX and discrete structures. The measured magnetic loss difference, $\Delta P_{\text{loss, mag}}$, is 1.56 W, demonstrating that the loss reduction offered by the ILX structure at this operating point is relatively small, in agreement with analytical loss evaluation. The thermocouple measurements are provided in Fig. 20, and the infrared thermal images are shown in Fig. 21. From Figs. 20 and 21, it can be observed that, for both the ILX and discrete structures, the transformer core reaches a higher temperature than the inductor core. The worst-case transformer temperature for both structures is 78 °C, as measured by the thermocouples. In contrast, the ILX inductor section reaches 50 °C, while the discrete inductor operates slightly cooler at 43 °C.

To validate the $\Delta P_{\text{loss, mag}}$ measurements, power converter losses are additionally measured using a WT500 YOKOGAWA

Authorized licensed use limited to: TU Delft Library. Downloaded on April 14,2026 at 08:54:41 UTC from IEEE Xplore. Restrictions apply.

TABLE VII
COMPARATIVE EXPERIMENTAL TEST RESULTS

Operating point (V_o, P_o)	Ambient temp (°C)	Discrete structure $P_{\text{loss,Disc}}$ (W)	ILX structure $P_{\text{loss,ILX}}$ (W)	Magnetic $\Delta P_{\text{loss,mag}}$ (W)	Converter efficiency with discrete (%)	Converter efficiency with ILX (%)	Converter $\Delta P_{\text{loss,conv}}$ (W)
450 V, 9 kW	4	164.6	150.1	14.5	96.82	96.96	13.0
450 V, 7 kW	4	143.33	133.27	10.06	96.83	96.95	9.0
450 V, 5 kW	4	110.34	102.62	7.72	96.27	96.36	5.0
450 V, 3 kW	4	30.94	23.93	7.01	93.24	93.36	4.8
387.5 V, 3 kW	25	75.54	73.98	1.56	97.19	97.30	3.5
350 V, 7 kW	4	91.05	82.89	8.16	97.38	97.47	7.0
250 V, 7 kW	4	47.43	41.26	6.17	96.31	96.53	16.0

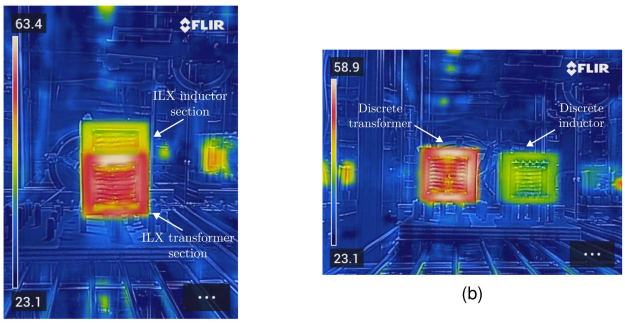

(a) (b)

Fig. 21. Steady-state infrared thermal image at 387.5 V, 3 kW, and 25 °C test condition for the (a) ILX structure and (b) discrete structures.

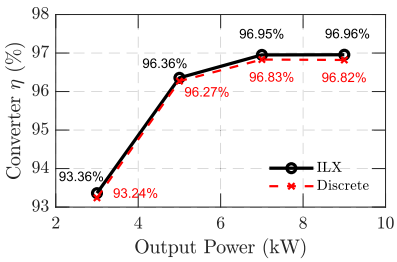

Fig. 22. DAB converter efficiency with ILX and a discrete structure for the test condition of V_o of 450 V, V_g of 775 V, and 4 °C ambient temperature over wide output power.

power analyzer, and the difference in converter-level losses between the ILX and discrete structures, $\Delta P_{\text{loss, conv}}$, is obtained. Table VII summarizes the magnetic and converter performance across the full operating voltage and output power range. It is observed that the converter-level loss difference, $\Delta P_{\text{loss, conv}}$, and the magnetic loss difference, $\Delta P_{\text{loss, mag}}$, show consistent agreement, indicating that the observed converter-level improvement is explained by the magnetics. Furthermore, Fig. 22 compares DAB converter efficiency with ILX and discrete structures at 450 V and 4 °C ambient temperature across a wide output power range. Here, it can be seen that the DAB converter with ILX structure achieves consistently higher efficiency than the discrete structure, prominently in the high power region.

VII. CONCLUSION

This work presented an integrated magnetic structure, ILX, for the DAB converter. ILX is assembled using off-the-shelf E-cores, which makes it practical and scalable. The ability to tune the series inductance without lowering the magnetizing inductance helps in avoiding excessive core losses. The weak coupling between the inductor and transformer windings of the ILX structure and the near-ideal coupling between the transformer primary and secondary windings have been first verified by FEM-based sensitivity analysis and subsequently validated through measurements. The presented analytical models and design methodology facilitate systematic ILX sizing for a given DAB converter specification. The peak-to-peak flux swing reduction in the shared core segment of the ILX structure, resulting from the presence of inductor and transformer fluxes, reduces core losses. The reduced core loss in the ILX structure is demonstrated using FEM simulation as well as experimental results. At 450 V, 9 kW operating point, a magnetic loss reduction of 8.8% has been obtained experimentally compared to the discrete structure, and this improvement is further reinforced by the higher converter efficiency measured with the ILX design. Future work aims to design thermal modeling of the ILX structure and design the cooling system accordingly.

REFERENCES

[1] G. Ortiz, J. Biela, and J. Kolar, "Optimized design of medium frequency transformers with high isolation requirements," in *Proc. 36th Annu. Conf. IEEE Ind. Electron. Soc.*, 2010, pp. 631–638.
[2] M. Mu, L. Xue, D. Boroyevich, B. Hughes, and P. Mattavelli, "Design of integrated transformer and inductor for high frequency dual active bridge GaN charger for PHEV," in *Proc. IEEE Appl. Power Electron. Conf. And Expo.*, 2015, pp. 579–585.
[3] M. Bakar and K. Bertilsson, "An improved modelling and construction of power transformer for controlled leakage inductance," in *Proc. IEEE 16th Int. Conf. Environ. Electric. Eng.*, 2016, pp. 1–5.
[4] B. Cougo and J. Kolar, "Integration of leakage inductance in tape wound core transformers for dual active bridge converters," in *Proc. 7th Int. Conf. Integr. Power Electron. Syst.*, 2012, pp. 1–6.
[5] T. Yuan, F. Jin, Z. Li, C. Zhao, and Q. Li, "Design of an integrated transformer with parallel windings for a 30-kW LLC resonant converter," *IEEE Trans. Power Electron.*, vol. 38, no. 11, pp. 14317–14333, Nov. 2023.
[6] M. Pavlovsky, S. Haan, and J. Ferreira, "Winding losses in high-current, high-frequency transformer foil windings with leakage layer," in *Proc. 37th IEEE Power Electron. Spec. Conf.*, 2006, pp. 1–7.
[7] J. Zhang, Z. Ouyang, M. Duffy, M. Andersen, and W. Hurley, "Leakage inductance calculation for planar transformers with a magnetic shunt," *IEEE Trans. Ind. Appl.*, vol. 50, no. 6, pp. 4107–4112, Nov./Dec. 2014.
[8] J. Biela and J. Kolar, "Analytic model inclusive transformer for resonant converters based on extended fundamental frequency analysis for resonant converter-design and optimization," in *IEEJ Trans. Ind. Appl.*, vol. 126, no. 5, pp. 568–577, 2006.
[9] E. Lee, J. Park, M. Kim, and S. Han, "An integrated transformer design with a center-core air-gap for DAB converters," in *IEEE Access*, vol. 9, pp. 121263–121278, 2021.

Authorized licensed use limited to: TU Delft Library. Downloaded on April 14,2026 at 08:54:41 UTC from IEEE Xplore. Restrictions apply.

[10] B. Li, Q. Li, and F. Lee, "High-frequency PCB winding transformer with integrated inductors for a bi-directional resonant converter," *IEEE Trans. Power Electron.*, vol. 34, no. 7, pp. 6123–6135, Jul. 2019.
[11] M. D'Antonio, S. Chakraborty, and A. Khaligh, "Planar transformer with asymmetric integrated leakage inductance using horizontal air gap," *IEEE Trans. Power Electron.*, vol. 36, no. 12, pp. 14014–14028, Dec. 2021.
[12] Y. Kim, C. Kim, K. Cho, K. Park, and G. Moon, "ZVS phase shift full bridge converter with separated primary winding," in *IEEE Energy Convers. Congr. Expo.*, 2009, pp. 484–489.
[13] Y. Liu, H. Wu, J. Zou, Y. Tai, and Z. Ge, "CLL resonant converter with secondary side resonant inductor and integrated magnetics," *IEEE Trans. Power Electron.*, vol. 36, no. 10, pp. 11316–11325, Oct. 2021.
[14] M. Ahmed, A. Nabih, F. Lee, and Q. Li, "Low-loss integrated inductor and transformer structure and application in regulated LLC converter for 48-V bus converter," in *IEEE J. Emerg. Sel. Topics Power Electron.*, vol. 8, no. 1, pp. 589–600, Mar. 2020.
[15] S. Stegen and J. Lu, "Structure comparison of high-frequency planar power integrated magnetic circuits," in *IEEE Trans. Magn.*, vol. 47, no. 10, pp. 4425–4428, Oct. 2011.
[16] Z. Cao et al. , "A low loss orthogonal decoupling magnetic integrated structure for dual active bridge converter," *IEEE Trans. Power Electron.*, vol. 37, no. 6, pp. 7013–7027, Jun. 2022.
[17] M. Iyer, "An approach towards extreme fast charging station architecture for electric vehicles with partial power processing," in Ph.D. thesis, Elect. Eng. North Carolina State Univ., Raleigh, NC, USA, 2020. [Online]. Available: https://repository.lib.ncsu.edu/items/2bf0b9de-e56d-4bb7-9d6a-b5a166bea293
[18] J. Muhlethaler, J. Kolar, and A. Ecklebe, "A novel approach for 3D air gap reluctance calculations," in *Proc. 8th Int. Conf. Power Electron.*, 2011, pp. 446–452.



Siddhesh Shinde (Graduate Student Member, IEEE) received the B.E. degree in electrical engineering from the University of Mumbai, Mumbai, India, in 2012, and the M.S. degree in power electronics from the University of Central Florida, Orlando, FL, USA, in 2016. He is currently working toward the Ph.D. degree in electrical engineering with the Delft University of Technology, Delft, The Netherlands.

From 2013 to 2014, he was a Project Engineer with the Indian Institute of Technology Bombay, Mumbai, India, contributing to the development of solar and battery-based microinverters funded by the Ministry of New and Renewable Energy, New Delhi, India. From 2017 to 2022, he was a Power Electronics Engineer with electric vehicle startups, including NIO and Lucid Motors, contributing to the development of automotive power converters. His research focuses on integrated magnetic structures and thermal design for high-power-density dc–dc converters in electric vehicle applications.



Gautam Rituraj (Member, IEEE) received the B.Tech. degree in electrical engineering from Uttar Pradesh Technical University, Lucknow, India, in 2012, and the Ph.D. degree in electrical engineering from the Indian Institute of Technology Guwahati, Guwahati, India, in 2021.

From 2021 to 2025, he was a Postdoctoral Researcher with TU Delft, Delft, The Netherlands, pursuing his research on off-grid EV charging, standalone microgrid design and optimization, hybrid energy storage integration, and electrolyzer systems. He is currently a Technical Staff Member with ESP Lab, DCE&S Group, Department of Electrical Sustainable Energy, Delft University of Technology, Delft, The Netherlands. His research interests include off-grid EV charging systems, electrolyzer systems, dc–dc converters, energy storage integration, analysis and design of wireless power transfer systems, coil design and modeling, and developing power electronic circuits for EV charging.

Dr. Rituraj was a recipient of the Gandhian Young Technological Innovation (GYTI) Appreciation 2021 for his doctoral work and holds one Indian patent. His paper was recognized as a featured article in IEEE OPEN JOURNAL OF THE INDUSTRIAL ELECTRONICS SOCIETY in 2023.



Gautham Ram Chandra Mouli (Senior Member, IEEE) received the bachelor's degree in electrical engineering from the National Institute of Technology Trichy, India, in 2011, the master's degree in electrical engineering from the Delft University of Technology, Delft, The Netherlands, in 2013, and the Ph.D. degree in electrical engineering from Delft University in 2018, for the development of a solar-powered V2G electric vehicle charger compatible with CHAdeMO, CCS/COMBO, and designed smart charging algorithms (with PRE, ABB, and UT Austin).

From 2017 to 2019, he was a Postdoctoral Researcher with TU Delft, Delft, The Netherlands, pursuing his research on power converters for EV charging, smart charging of EVs, trolley busses. He is currently an Associate Professor in the d systems, Energy Conversion and Storage Group, Department of Electrical Sustainable Energy, Delft University of Technology. He is the Coordinator and a Lecturer for the Massive Open Online Course (MOOC) on Electric cars on edX.org with 175 000 learners from 175 countries. His research interests include electric vehicle charging, PV systems, power electronics, and intelligent control.

Dr. Chandra Mouli was recipient of the best paper prize in the IEEE TRANSACTIONS ON INDUSTRIAL INFORMATICS in 2018, the Best Poster prize at Erasmus Energy Forum 2016, The Netherlands, and the Best Paper prize at the IEEE INDICON Conference 2009, India. He was also the recipient of the "Most significant innovation in electric vehicles" award from IDtechEx in 2018 and the "Best Tech Idea of 2018" by KIJK. He is involved in many projects with industrial and academic partners at national and EU level concerning electric mobility and renewable energy, such as PV charging of electric vehicles, OSCD, Trolley 2.0, Flexgrid, Flexinet, and NEON.



Vishnu Mahadeva Iyer (Senior Member, IEEE) received the B.Tech. degree in electrical and electronics engineering from the College of Engineering, Trivandrum, India, in 2011, the M.E. degree from the Indian Institute of Science (IISc), Bengaluru, India, in 2013, and the Ph.D. degree from NC State University, Raleigh, NC, USA, in 2020, both in electrical engineering.

In 2020, he was a Lead Engineer with GE Aerospace Research, Niskayuna, NY, USA, and a Power Electronics Engineer with GE Research, Bengaluru, India, from 2013 to 2015. In September 2020, he was an Assistant Professor with the Department of Electrical Engineering, IISc Bengaluru. His research interests include resonant and soft-switched power converters, high-frequency magnetics, control and stability of power electronic converters, and partial power processing.



Pavol Bauer (Senior Member, IEEE) received the master's degree in electrical engineering from the Technical University of Kosice, Slovakia, in 1985, and the Ph.D. degree from in electrical engineering from Delft University of Technology, in 1995. He is currently a Full Professor with the Department of Electrical Sustainable Energy, Delft University of Technology, Delft, The Netherlands, and the Head of DC Systems, Energy Conversion, and Storage group. He is also honorary Professor with Politehnica University Timisioira, Timisioira, Romania. From 2002 to 2003, he was working with KEMA (DNV GL, Arnhem) on different projects related to power electronics applications in power systems. He has authored or coauthored more than 170 journal and more than 500 conference papers in his field (with H factor Google scholar 60, Web of Science 40). He has authored or coauthored eight books, holds ten international patents and organized several tutorials at the international conferences. He has worked on many projects for industry concerning wind and wave energy, power electronic applications for power systems, such as Smarttrafo; HVDC systems, projects for smart cities, such as PV charging of electric vehicles, PV and storage integration, contactless charging; and he participated in several Leonardo da Vinci, H2020 and Electric Mobility Europe EU projects as Project Partner (ELINA, INETELE, E-Pragmatic, Micact, Trolly 2.0, OSCD, P2P, Progressus, Tulip, Flow) and Coordinator (PEMCWebLab.com-Edipe, SustEner, Eranet DCMICRO). His research focuses on power electronics for charging of electric vehicles and dc grids.

Dr. Bauer was the recipient of the title prof. from the president of Czech Republic at the Brno University of Technology, Brno, Czechia, (2008), and the Delft University of Technology (2016), and also the recipient of honorary doctorate (Dr.h.c).

Authorized licensed use limited to: TU Delft Library. Downloaded on April 14,2026 at 08:54:41 UTC from IEEE Xplore. Restrictions apply.